Cell Traction Forces Direct Fibronectin Matrix Assembly

Christopher A. Lemmon,[†] Christopher S. Chen,[‡] and Lewis H. Romer[†§*]

[†]Departments of Biomedical Engineering and Anesthesiology and Critical Care Medicine, The Johns Hopkins University School of Medicine, Baltimore, Maryland; [‡]Department of Bioengineering, University of Pennsylvania, Philadelphia, Pennsylvania; and [§]Departments of Cell Biology, Pediatrics, and Center for Cell Dynamics, The Johns Hopkins University School of Medicine, Baltimore, Maryland

ABSTRACT   Interactions between cells and the surrounding matrix are critical to the development and engineering of tissues. We have investigated the role of cell-derived traction forces in the assembly of extracellular matrix using what we believe is a novel assay that allows for simultaneous measurement of traction forces and fibronectin fibril growth at discrete cell-matrix attachment sites. NIH3T3 cells were plated onto arrays of deformable cantilever posts for 2–24 h. Data indicate that developing fibril orientation is guided by the direction of the traction force applied to that fibril. In addition, cells initially establish a spatial distribution of traction forces that is largest at the cell edge and decreases toward the cell center. This distribution progressively shifts from a predominantly peripheral pattern to a more uniform pattern as compressive strain at the cell perimeter decreases with time. The impact of these changes on fibrillogenesis was tested by treating cells with blebbistatin or calyculin A to tonically block or augment, respectively, myosin II activity. Both treatments blocked the inward translation of traction forces, the dissipation of compressive strain, and fibronectin fibrillogenesis over time. These data indicate that dynamic spatial and temporal changes in traction force and local strain may contribute to successful matrix assembly.

INTRODUCTION

Interactions between cells and the surrounding extracellular matrix (ECM) are critical for optimal cell migration, spreading, differentiation, and tissue morphogenesis. Successful assembly of an organized ECM requires precisely controlled interactions at the cell-matrix interface. Fibronectin is a major component of ECM that is critical during development and is crucial to survival. Fibronectin knockout mice die at stage E8.5 (1). In its soluble form, fibronectin is present as an inactive dimer. Attachment of the inactive dimer to the cell surface is recognized as the first step in fibril assembly. The binding of fibronectin to the cell surface occurs through members of the β_1 integrin family, primarily via the $\alpha_5\beta_1$ heterodimer. Fibronectin is then assembled into fibrils (2), which are anchored to the ECM substrate at the cell periphery and are cell-bound near the center of the cell (3). Assembled fibrils are bundles of fibronectin (FN) molecules, which can range from 5 to 1000 nm in diameter (4,5). The fibrils are elastic and mobile, allowing them to move with the cell. The FNIII domains of fibronectin are folded into seven-stranded β-sandwiches. The first FNIII domain contains a cryptic binding domain (6,7), which, when the fibronectin molecule is under tension, may be exposed and facilitate intermolecular association and fibril growth (6,8,9).

Fibronectin fibrils demonstrate elastic properties, stretching and relaxing in response to cell movements (10), as they grow and elongate along assembled F-actin filaments (3). Rho activation stimulates cytoskeletal contractility and the bundling of actin stress fibers (8), and evidence suggests that fibronectin fibrillogenesis is also regulated by cytoskel-etal contraction (11). The mechanism of fibronectin fibril elongation is still debated. Some data suggest that FNIII domains unfold under cell-generated forces (12,13), whereas others suggest a conformational change of fibronectin without domain unfolding (14,15).

Adherent cells generate tension via contraction of the actin cytoskeleton and transmit this force via focal adhesions to the underlying substrate (16). This was first demonstrated by plating adherent cells onto a thin layer of polydimethylsiloxane (PDMS). Forces exerted by cells were visualized as wrinkles in the deformable substrate (17,18). Quantification of forces on deformable substrates was later achieved by embedding fluorescent beads within the substrate and tracking bead location before and after contraction (19). This system was used to demonstrate that the magnitude and direction of traction forces correlated with the size and direction of the adhesion to which the force was applied. An alternative system for traction force measurement consists of a substrate of deformable cantilevers that are deflected by cell contraction (20). The advantage of this system is that each cantilever acts as an individual micromechanosensor at a discrete cell attachment site.

In this study, we have directly investigated the relationship between cytoskeletal contraction and the assembly of fibronectin fibrils using microfabricated post-array detectors (mPADs) to simultaneously measure fibril size and cell-derived traction forces. Our data indicate that traction forces guide the direction of developing fibronectin fibrils, and that fibrillogenesis is driven by the spatial redistribution of traction forces from the cell periphery toward the cell center and the relaxation of centripetally directed compressive strain at the cell perimeter.

MATERIALS AND METHODS

Cell culture and reagents

Stably transfected NIH3T3 cells expressing YFP-fibronectin were a gift from Dr. Harold Erickson (Duke University, Durham, NC). Cells were cultured in DMEM (Sigma, St. Louis, MO) containing 10% fetal bovine serum (Atlantic Biological, Elizabeth City, NC), 1% glutamine, and 1% penicillin/streptomycin under standard culture conditions.

Microfabricated post-array detectors

mPADs consist of uniformly spaced grids of deformable silicon posts. Fabrication of mPAD substrates was described previously (20,21). Briefly, an mPAD template was made by pouring PDMS over an array of posts lithographically generated on a silicon wafer from an epoxy-type, near-UV photoresist (SU-8, Shell Chemical, Geismar, LA). The mPAD template was cured overnight at 110°C, peeled from the SU-8 post array, oxidized for 1 min, and treated with (tridecafluoro-1,1,2,2-tetrahydrooctyl)-1-trichlorosilane vapor overnight under vacuum to aid removal of mPADs from the template. mPADs were then made by pouring PDMS onto the template, degassing under vacuum, and curing overnight at 100°C. mPAD post stiffness was measured using calibrated glass needles (World Precision Instruments, Sarasota, FL) on an original mPAD with 11-μm post height and scaled to an appropriate value for 10-μm posts. Surface-oxidized mPADs were then microcontact-printed with fibronectin from a PDMS stamp precoated with 50 μg/ml human plasma fibronectin (Sigma) to promote cell adhesion to mPAD post top surfaces. mPADs were coated first with 0.5 μg/ml BSA-647 (Invitrogen Molecular Probes, Carlsbad, CA) to facilitate volumetric imaging of the posts, followed by 1% Pluronics F-68 (BASF, Florham Park, NJ) to prevent cell adhesion. mPAD posts were 3 μm in diameter, 10 μm tall, and spaced 9 μm apart. For experiments in which cell contractility was altered, cells were plated onto posts for 90 min to allow initial adhesion. Subsequently, cells were treated with either 100 nM Calyculin A or 20 μM blebbistatin for the duration of the experiment.

Immunofluorescence

Cells cultured on mPADs were fixed and permeabilized with 3% paraformaldehyde and 0.5% Triton X-100 in PBS, rinsed with PBS, incubated with a polyclonal antibody against fibronectin (Abcam, Cambridge, MA), and detected with fluorophore-conjugated isotype-specific and affinity cross-adsorbed anti-IgG antibodies (Millipore Chemicon, Temecula, CA). Filamentous actin was visualized by incubating samples with fluorophore-conjugated phalloidin (Molecular Probes). Images were acquired using epifluorescence microscopy (Eclipse 200, Nikon, Melville, NY) with a 60× objective, Openlab software (Improvision, Lexington, MA), and an internally cooled 12-bit CCD camera (CoolSnapHQ, Photometrics, Tucson, AZ).

Image acquisition and data analysis

Acquired images were exported as 16-bit TIFF images and read into an original Matlab (The MathWorks, Natick, MA) code written by the authors and designed to analyze mPAD post deflections, as previously described (21). Briefly, acquired images were imported, and a thresholding algorithm was used to determine cell area, detect cell edges, and define mPAD post centroids. Deflections were calculated and vector plots of the resulting cell-generated forces were assembled. All analysis was performed using our original code in Matlab on a 2.4 GHz Pentium 4 PC with 2 GB RAM.

Measurement of fibronectin fibril size

Quantification of matrix assembly from immunofluorescence images required development of algorithms to measure fibronectin fibrils independently of microcontact-printed fibronectin. Fibronectin images were converted to a binary image based on a threshold value calculated using the "graythresh" function in the Matlab Imaging toolbox (The Mathworks). The graythresh function uses the ad hoc algorithm to determine an appropriate threshold that minimizes the intraclass variance of the thresholded black and white pixels (22). Perinuclear fibronectin was identified as round, punctate dots that did not terminate at mPAD posts. These were removed from binary images. The resulting images contained both cell-assembled and microcontact-printed fibronectin areas. Microcontact-printed FN was quantified by calculating the average fibronectin area of unoccupied mPAD posts and was subtracted from all cell-occupied post fibronectin measurements.

Strain methods and equations

Strain in each rectangular four-point element was calculated in both the x and y directions:

$$\varepsilon_x = \frac{x_f - x_i}{x_i} \quad \varepsilon_y = \frac{y_f - y_i}{y_i},$$

where x_f and y_f are the average element lengths in the contracted state, and x_i and y_i are the average element lengths in the relaxed state. γ_{xy} is also calculated as the torsion angle between the contracted and relaxed states (see Fig. 4 A). Strains can then be transformed to any arbitrary coordinate system if 2-D plan strain is assumed. The transformed strains ε_x', ε_y', and γ_{xy}' were calculated from the untransformed strains (see Fig. 7 A):

$$\varepsilon_x' = \frac{\varepsilon_x + \varepsilon_y}{2} + \frac{\varepsilon_x - \varepsilon_y}{2}\cos 2\theta + \frac{\gamma_{xy}}{2}\sin 2\theta$$

$$\varepsilon_y' = \frac{\varepsilon_x + \varepsilon_y}{2} - \frac{\varepsilon_x - \varepsilon_y}{2}\cos 2\theta - \frac{\gamma_{xy}}{2}\sin 2\theta$$

$$\gamma_{xy}' = -\left(\varepsilon_x - \varepsilon_y\right)\sin 2\theta + \gamma_{xy}\cos 2\theta.$$

In this work, untransformed strains (see Fig. 7, B and C) were transformed using a unique θ for each element that was given by the angle between the original x axis of the mPADs and the vector pointing toward the cell centroid (see Fig. 7 D).

RESULTS

Simultaneous measurement of fibronectin assembly and traction force

We have developed an assay that simultaneously and quantitatively examines contractile forces, cell size, and fibronectin fibrillogenesis. This was done by using a previously described array of uniformly spaced, polydimethylsiloxane (PDMS) cantilever posts that bend when a force is applied to the free end (20,21). The mPADs were prepared such that cell adhesion was restricted to the top surface of each detergent-coated mPAD post by microcontact printing of fibronectin. As cells contracted, the mPAD posts bent in response, and the force was calculated by measuring the deflection of each mPAD post (Fig. 1 A). Deflections of the mPADs (Fig. 1 B, *white arrows*) were quantified from the differences between the centroid positions near the apical (free) (Fig. 1 B, *blue circles*) and basal (anchored) (Fig. 1 B, *red circles*) ends of the posts. This resulted in a map of the traction forces generated by the cell (Fig. 1 C). Microcontact-printed fibronectin on the top of each post also served as an attachment site for cell-derived fibronectin fibril
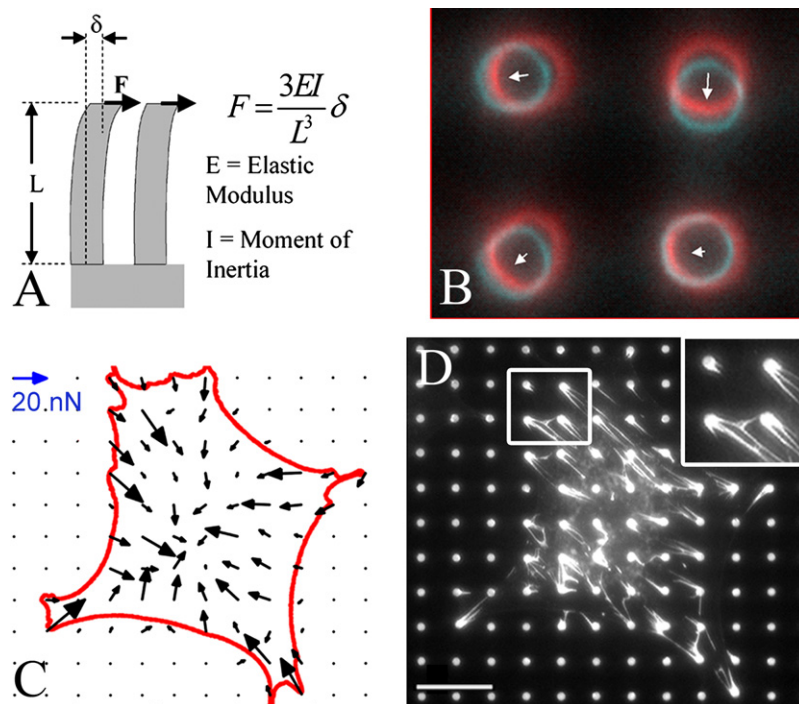
FIGURE 1 Simultaneous measurement of fibronectin fibrillogenesis and traction force. (A) Traction forces were quantified by measuring the deflections of mPAD posts. The stiffness of the posts was empirically measured, but can also be estimated from beam bending theory using the equation shown. The mPAD posts are 10 μm tall, 3 μm in diameter, and have a post-to-post spacing of 9 μm. (B) mPAD posts are coated with fluorophore-labeled BSA to facilitate volumetric imaging of the entire length of the post. Images were acquired near the base of the posts (red circles) and near the top of the posts (blue circles). The magnitude and direction of the force vector is calculated from the deflection of the post centroids from the base to the top image (white arrows). (C) Traction force vectors (black arrows) at each post were assembled into a map of cell-generated traction forces with the cell perimeter shown in red. Blue reference vector, 20 nN. (D) Immunofluorescence images of fibronectin indicate the presence of cell-derived fibronectin fibrils extending from each post. These images were used to quantify the degree of fibronectin fibril formation. Scale bar, 20 μm.

formation (Fig. 1 D). The size of fibronectin fibrils associated with each mPAD post was quantified using our original Matlab-based image-processing program (available at www.hopkinsmedicine.org/anesthesiology/research/mpadtools). Fibronectin immunofluorescence images were subjected to a thresholding function to generate a binary image. Perinuclear fibronectin was removed from the binary image based on proximity to the nucleus and lack of fibrillar shape. The region of the binary image associated with each mPAD post was then summed to calculate the total fibronectin-occupied area associated with that mPAD post. The average fibronectin area associated with mPAD posts not contacted by a cell (and thus free of cell-derived fibrils) was subtracted from all fibronectin areas to account for microcontact-printed fibronectin. Traction forces and fibronectin fibril size data were normalized for cell size by correcting for the number of mPAD posts occupied by each cell. The discontinuous surface of the mPADs allows for a unique perspective on the interaction between cell traction force and ECM assembly: both the force magnitude and direction, and the fibronectin fibril size and orientation were analyzed for each discrete attachment site.

Traction force dictates the direction of fibrillogenesis at individual points of cell-matrix adhesion

Previous data suggest a link between actomyosin-driven cell contractility and the assembly of fibronectin fibrils (10,13,15,23,24); however, the mPADs allow for a more precise definition of the relationship between the two. Studies were done in two stages: first, we determined whether the direction of the pulling force dictated the direction of fibril growth. NIH3T3 cells were plated onto mPADs for 24 h, and the direction of the major axis of the fibronectin fibril and the direction of the applied force vector for each mPAD post were calculated. Orientation of the major axis of fibronectin fibrils was plotted against the direction of the applied traction force vector ($N = 1036$ posts from 20 cells), indicating a strong linear relationship between the two ($R^2 = 0.7404$) (Fig. 2). We next investigated the question of whether local force magnitude determined fibril size. Results indicated that there was no correlation between the magnitude of local force and the size of the fibronectin fibril (Fig. 2 C). This demonstrates that the relationship between cell traction force and matrix assembly is not a simple linear relationship. This could be explained by a combination of static and mobile cell-matrix adhesions applying force to the mPAD posts, by fixation artifact, or by a more complex and dynamic relationship between cell traction force and fibronectin fibrillogenesis. Data in Fig. S2 in the Supporting Material suggest that fixation did not alter cell force measurements, and the dynamics and topography of the interplay between cell traction force and fibril patterning was examined.

Temporal and spatial changes in cellular traction forces during fibronectin assembly

An analysis of force vectors at individual posts at a single point in time indicated a strong relationship between traction force direction and fibril direction, but not between traction force magnitude and fibril size. However, these studies did not account for differences in patterns of force generation
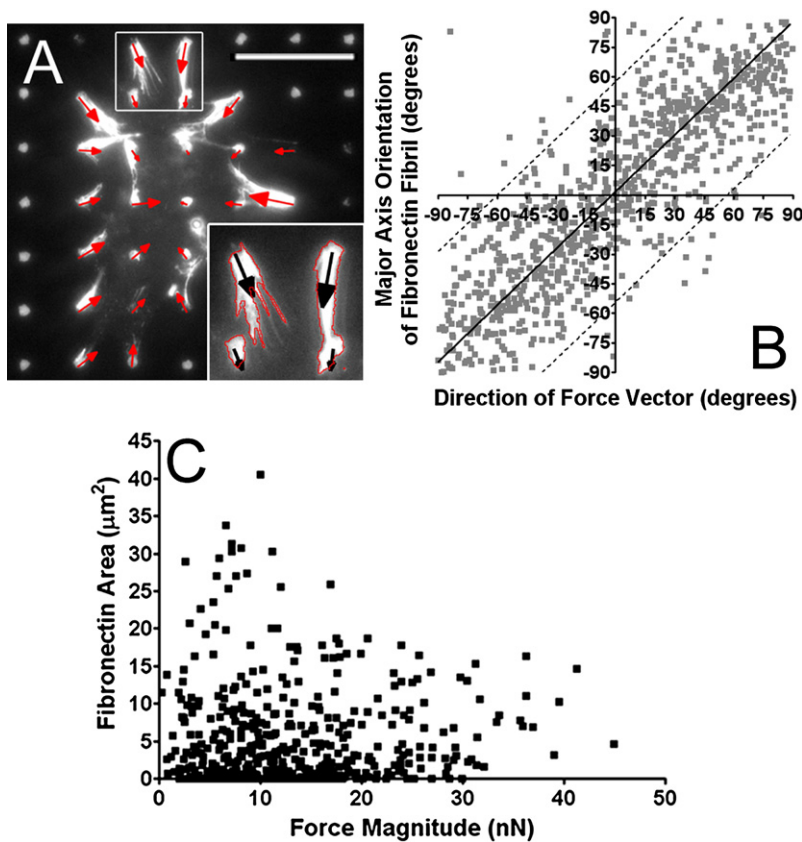
FIGURE 2 Relationship between size and orientation of fibronectin fibrils and magnitude and direction of the traction forces applied to that fibril. The relationship between the size and orientation of a developing fibronectin fibril and the traction vector applied to that vector was investigated by analyzing data from individual mPAD posts. (*A*) A representative image of fibronectin fibrils and the corresponding traction force vectors (*red arrows*; *black arrows* in inset) demonstrates the relationship between fibronectin fibril orientation and traction force direction. Fibronectin immunofluorescence is shown in white, and the outline of quantified fibrils calculated by our image-processing algorithm is shown in red in the inset. Scale bar, 20 μm. (*B*) Orientation of the major axis of fibronectin fibrils was plotted against the direction of the applied traction force vector ($N = 1036$ points from 20 cells). (*C*) Measurements of cell on mPADs at isolated time points (24 h) showed no relationship between traction force magnitude and fibronectin fibril size.

that might occur over the time that fibronectin fibrillogenesis is occurring, or for spatial variations in traction force magnitude across a cell. We examined these issues by plating NIH 3T3 cells onto mPADs for varying lengths of time and examining the degree of fibronectin assembly and the distribution of traction forces at each time point. Traction force maps, actin images, and fibronectin images are shown for cells at 2 h, 9 h, and 18 h (Fig. 3, *A–C*, respectively). Graphs summarizing changes in cell surface area, total force per cell, and force per post data over the entire study period were also prepared (Fig. S1). A change in the distribution of traction forces was observed with time, shifting from a predominance of traction forces at the cell periphery in hours 2–3 to an increase in traction forces closer to the cell center in hours 9–10. To quantify this redistribution of forces, traction forces were partitioned into ''peripheral forces'', which are indicated by black arrows in the traction force maps, and ''interior forces'', which are indicated by red arrows in the traction force maps (Fig. 3, *A–C*). Forces located one post diameter from the cell edge were defined as ''peripheral''. All other vectors were categorized as ''interior'' forces. This segregation was used to calculate the percentage of the total cell force that was generated at either the cell edge or beneath the interior regions of the cell (Fig. 3 *D*). These analyses indicated that the percentage of total force generated toward the cell center was initially low, but increased 2.5-fold over the first 10 h of plating. This increase in the percentage of force

beneath the interior of the cell corresponded with a rapid rise in fibronectin fibril size (Fig. 3 *D*). The increase in interior force percentage also preceded subsequent increases in cell size, indicating that these effects were not driven by cell spreading (Fig. 3 *E*). After 10 h, cells exhibited an oscillatory pattern in which both the percentage of total force accounted for by interior forces and the average fibronectin fibril size rose and fell. Growth of fibronectin fibrils appeared to follow increments in interior force after a lag period of ~2 h (Fig. 3 *D*), but finer time points would be needed to precisely define this lag. A plausible explanation for these results would be that a relationship exists between the translation of traction forces from the cell periphery to the cell center and the assembly of fibronectin fibrils.

Decoupling of cell spreading and interior force percentage

During the time of maximal fibronectin assembly, there are increases in both interior force percentage and cell size. We examined the temporal relationship between these two measurements to determine whether increases in interior force percentage were mediated by cell spreading. Temporal data indicate that the rise in interior force percentage precedes increases in cell size (Fig. S1). To further examine the relationship, we plotted interior force percentage as a function of cell size for time points between 4.5 and 12 h
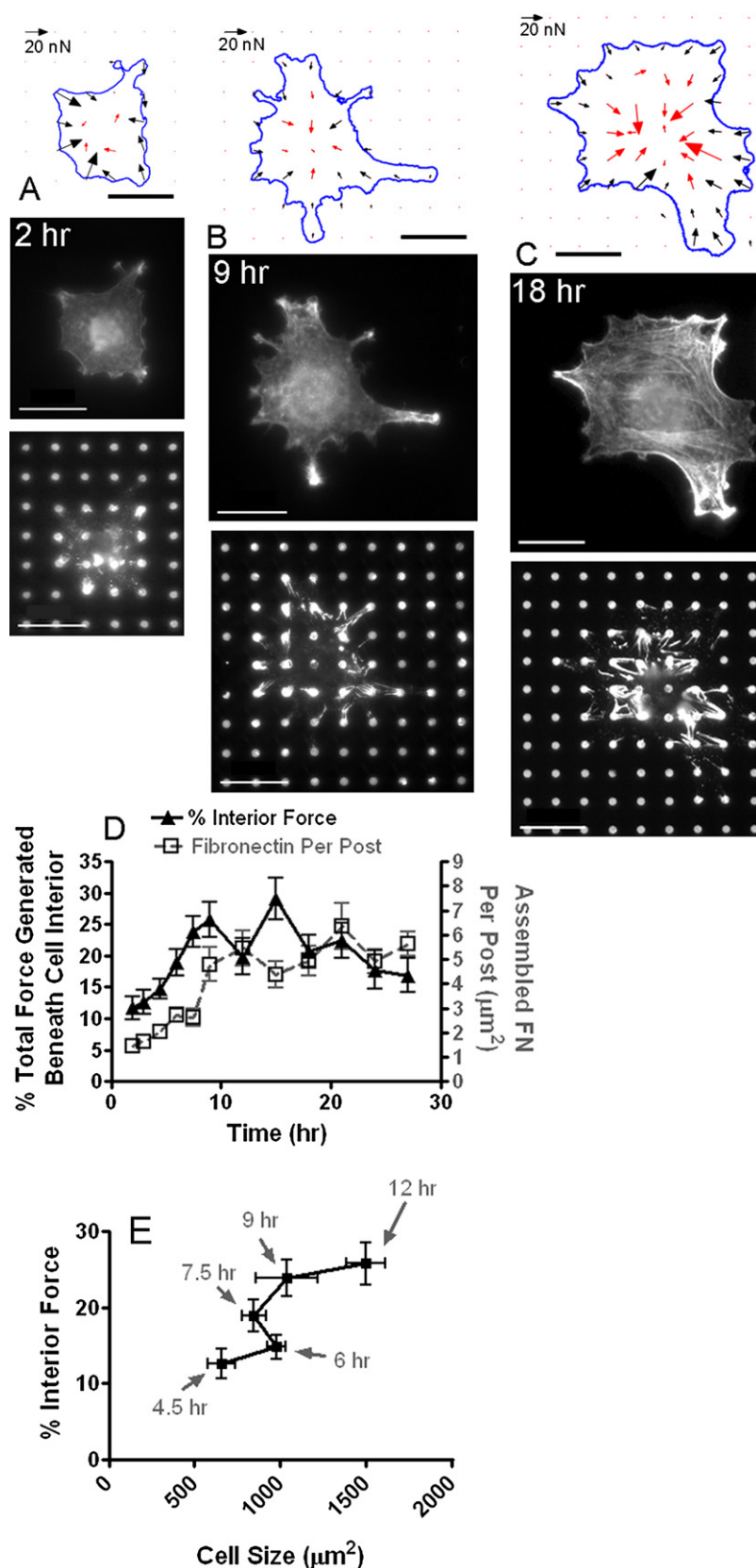
FIGURE 3 Spatial redistribution of traction forces as a function of time. NIH3T3 cells were plated onto mPADs for 2–24 h. (*A–C*) Traction force maps (*upper*), actin epifluorescence (*middle*), and fibronectin immunofluorescence (*lower*) from representative cells at 2 h (*A*), 9 h (*B*), and 18 h (*C*), respectively, after plating. Traction forces were initially large at the cell periphery (*black vectors*) and small toward the cell center (*red vectors*), but progressed toward a pattern with smaller peripheral vectors and larger interior vectors. Scale bars in immunofluorescence images, 20 μm. Scale vectors in traction force maps, 20 nN. (*D*) The percentage of total cell force generated away from the cell periphery (*black*) increased with time over the first 10 h of plating and then oscillated with continued time in culture. Fibronectin fibril size (*gray*) fluctuated in accordance with the changes in the percentage of interior force. Each time point is an average of data from $N = 9$–20 cells. Bars represent the mean $\pm$ SE. (*E*) Interior force percentage was plotted against cell size for cells plated onto mPADs for 4.5, 6, 7.5, 9, and 12 h (*gray arrows*). Data indicate that cell size remained constant during this period of largest increase in interior force percentage (6–9 h).

(Fig. 3 *E*). This window of time brackets the time of maximal matrix assembly. Results indicated that the interior force percentage increased between 6 and 9 h with no significant change in cell size. Subsequently, cell spreading occurred between 9 and 12 h with no significant changes in interior force percentage.

Changes in subcellular strain predict fibronectin fibrillogenesis

Our time course data suggested that the progression of traction forces from the cell periphery toward the cell interior over time may drive fibronectin fibrillogenesis. We next asked whether there was a subcellular quantification of traction force translocation that could be used as an indicator of fibronectin assembly. To begin, we used traction force maps to calculate the apparent strain in rectangular finite element quadrants. Quadrants were defined by four mPAD posts such that the corner of each aligned with an mPAD post. The contracted state of each element was generated from the deflected positions of each of the four mPAD posts, whereas the relaxed state was generated from the undeflected positions of the same four posts. Axial strains (ε_x and ε_y) and torsional strain (γ_{xy}) were calculated along the *x* and *y* axes associated with the grid layout of the mPAD using plane strain equations (Fig. 4 *A*). Since Rho kinase- and myosin light chain kinase-driven contraction (25) and fibronectin fibril growth (3) all proceed in a centripetal direction, the strain in each region was calculated in the direction pointed toward the cell centroid. Strains were transformed to correspond to this centripetally directed axis (Fig. 4 *B*), defined by the vector from the center of each quadrant to the cell centroid using transform equations for 2D plane strain. Tensile strains (quadrant elongation) are represented by positive values, whereas compressive strains (quadrant shortening) are represented by negative values. Equations and further explanation of this analysis are provided in Materials and Methods. Similar to our analysis of traction forces, strains were separated into peripheral strains and interior strains. The percentage of each region occupied by assembled fibronectin was calculated and compared with strain maps. Results indicated that strains at the peripheral regions of the cell were initially compressive, that the strain in these quadrants progressively relaxed, and that the dissipation of compressive strain corresponded with an increase in assembled fibronectin (Fig. 4 *G*). This can be seen in the representative NIH3T3 fibroblasts plated onto mPADs for 3 h (Fig. 4, *C* and *D*) and 24 h (Fig. 4, *E* and *F*). These data suggest that dynamic changes in strain from compressive to neutral may play a role in the assembly of fibronectin fibrils.

Effects of myosin-driven contractility on subcellular strain and fibronectin fibrillogenesis

NIH 3T3 cells exhibited a compression of peripheral subcellular regions at early time points, followed by a relaxation of these regions and a corresponding assembly of fibronectin. This would indicate that neither global tonic contraction nor global tonic relaxation of the cytoskeleton would potentiate fibronectin fibrillogenesis; that is, either inhibition or activation of the contractile machinery should eliminate the strain gradients and impair matrix assembly. To investigate this hypothesis, we modulated actomyosin contractility by perturbing the function of nonmuscle myosin II. NIH3T3 cells were plated onto mPADs and treated with either 20 μM blebbistatin to inhibit myosin II (26) or 100 nM calyculin A to inhibit myosin light chain phosphatase and thus increase myosin light chain phosphorylation (27). Cells were fixed at 3, 9, or 24 h after initial plating. Quantification of cell traction forces confirmed that the average traction force per post was increased in calyculin-A-treated cells and decreased in blebbistatin-treated cells (Fig. 5 *A*). Treatment with either calyculin A or blebbistatin inhibited the temporal redistribution of traction forces, as indicated by the absence of change in the percentage of force generated beneath the cell interior (Fig. 5 *B*). Both treatments also eliminated the time-dependent changes in compressive strain at the cell edge that were seen in the control condition (Fig. 5 *C*). The mean strain in blebbistatin-treated cells was tensile at all times, whereas the mean strain in calyculin-A-treated cells was consistently compressive and did not show much relaxation. Treatment with either blebbistatin or calyculin A led to nearly complete ablation of fibronectin assembly (Fig. 5 *D*), indicating that generalized tonic changes in the contractile state of the cell (i.e., either up or down) impaired fibrillogenesis equally. These observations support the hypothesis that dynamic temporal changes in traction force distribution and changes in peripheral strain from compressive to neutral support successful fibronectin fibrillogenesis.

DISCUSSION

Recent studies from multiple disciplines highlight the importance of mechanical interactions between cells and their surrounding extracellular environment (28,29). Mechanistic insights into cellular regulation and integration of cell-matrix adhesion and cytoskeletal dynamics during the assembly and rearrangement of ECM are critical to a working understanding of tissue morphogenesis, tissue engineering, and regenerative medicine. In this work, we present what we believe is a novel assay that allows for simultaneous measurement of cell-generated traction forces and fibronectin fibril formation. We have demonstrated several parameters of the cell traction force field that change during matrix assembly. First, we have shown that the traction force vector applied by a cell to a growing fibronectin fibril dictates the direction of that growing fibril. Second, we have shown that measurable increases in fibronectin fibril size occur after a transition from a peripherally dominant traction force pattern to a more balanced distribution of forces that is associated with an increase in forces close to the cell center. This
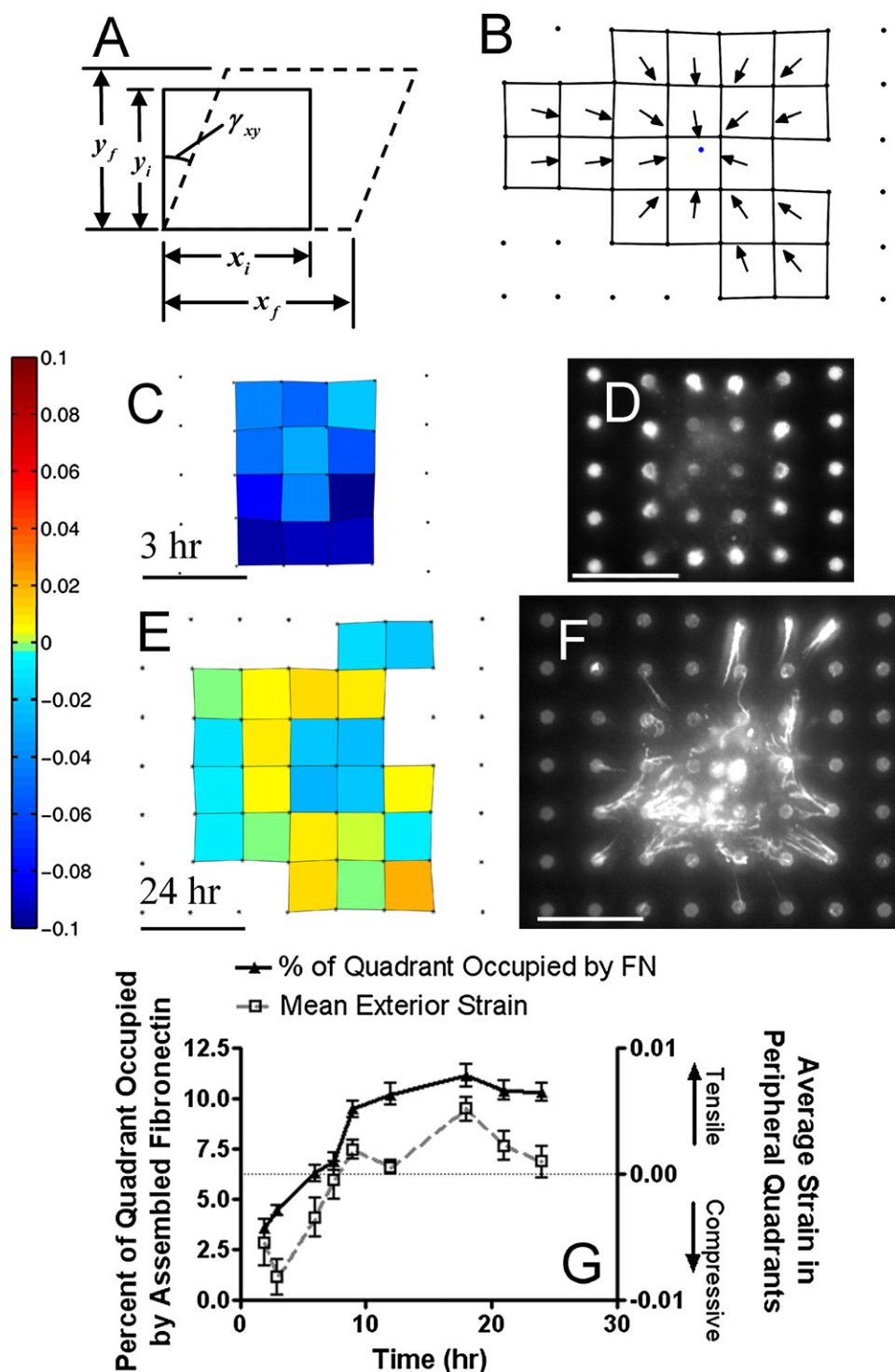
FIGURE 4 Relationship between subcellular strain and fibronectin assembly. Subcellular strain was calculated in quadrants defined by four mPAD posts at multiple time points. (*A*) The three components of plane strain were calculated in the *x*- and *y*-coordinates that correspond to the axes of the mPADs. (*B*) Strains in each quadrant were transformed to correspond with axes directed toward the cell centroid (*black arrows,* direction of strain axes; *blue dot,* centroid). (*C* and *D*) A representative strain map (*C*) and a fibronectin immunofluorescence image (*D*) from a 3T3 fibroblast plated onto an mPAD for 3 h. (*E* and *F*) A representative strain map (*E*) and a fibronectin image (*F*) from an NIH3T3 fibroblast plated onto an mPAD for 24 h. The color map along the lefthand border is for both strain maps (*C* and *E*). Scale bars in immunofluorescence images, 20 μm. (*G*) The average strain in peripheral cell regions and the percentage of each region occupied by assembled fibronectin was calculated for each time point. Bars represent mean $\pm$ SE. Each time point represents the average data from $N = 9$–20 cells.

transition of traction force patterns from peripherally dominant to more uniformly distributed is not unique to cells spreading on the mPAD system—it is also seen in cells spreading on planar sheets of polyacrylamide (30). Third, this centripetally directed translation of force is accompanied by the progressive relaxation of compressive strain at the cell perimeter. Thus, matrix assembly apparently may involve initial compressive strain of peripheral regions of the cell that is followed by a process of graded relaxation within these same regions. Perturbations of the normal regulation of nonmuscle myosin II support the hypothesis that dynamic changes in traction force patterns occur during fibronectin fibrillogenesis, since tonically increased and decreased contractility both prevent matrix assembly.
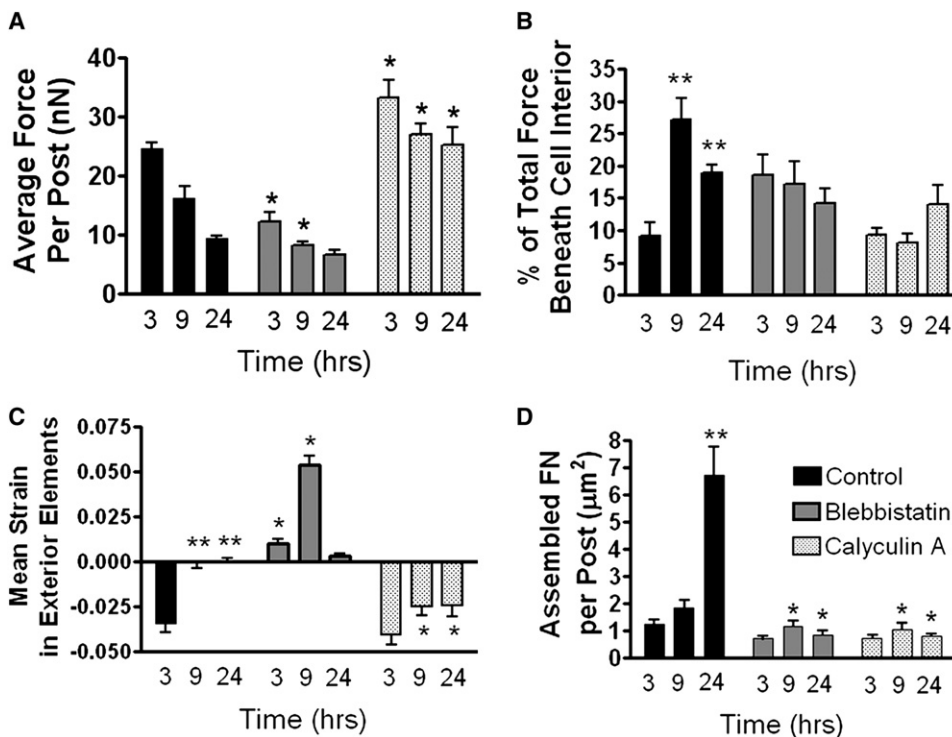
FIGURE 5 Effects of myosin II on traction force distribution and matrix assembly. NIH3T3 cells were plated for 3, 9, or 24 h and treated with either blebbistatin (20 μM) or calyculin A (100 nM). (*A*) The average force per mPAD post at all time points was reduced in blebbistatin-treated cells and elevated in calyculin-A-treated cells compared to untreated cells. Calculation of the average force per post allowed for comparison of traction forces independent of cell size. (*B*) The percentage of force generated away from the cell periphery increased with time in control cells. This redistribution of forces was not seen in either blebbistatin- or calyculin-A-treated cells. (*C*) The average strain in exterior regions of the cell changed with time from compressive toward neutral in control cells, but this transition was abolished in both blebbistatin- and calyculin-A-treated cells. (*D*) The average fibronectin fibril area per mPAD post was sharply reduced in response to treatment with either blebbistatin or calyculin A. Bars represent mean $\pm$ SE. *$p < 0.05$ versus control at the same time point, **$p < 0.05$ versus 3-h control ($N > 10$ cells for each time point and condition).

Of particular interest is the way in which subcellular strain may mitigate fibronectin fibrillogenesis. We hypothesize a mechanism by which local fluctuations in strain dictate fibril growth. Initial contraction of peripheral regions is accompanied by a lack of contraction by central regions (Fig. 6 *A*), resulting in compressive strain in these regions, which may initiate clustering of fibronectin. This differential contractility could occur by spatial segregation of contractile machinery, such as restricted localization of nonmuscle myosin II isoforms (31,32). It may also be regulated by local variations in cytoskeletal stiffness. For example, increased microtubule density in nonperipheral regions of the cell may resist contractile forces (33), whereas peripheral regions may contract more in the absence of this compact microtubule structure. Subsequently, traction forces away from the cell edge increase while peripheral traction forces relax (Fig. 6 *B*). This transition of peripheral strain from compressive to neutral could support the pulling of nascent fibronectin clusters into fully developed fibronectin fibrils. Our findings support those of of others who suggest that cytoskeletal strain is regulated at a circumscribed subcellular level (34), and that there may be discrete minimum functional units of cytoskeletal organization that are competent to perform fibrillogenesis.

Our observations that changes in the spatial distribution of force with time occur during cell spreading and are needed for optimal matrix assembly are consistent with previous work. Reinhart-King et al. found that cell attachment sites near the perimeter contributed a smaller percentage of cell traction force as cell spreading and time progressed. In addition, Cai et al. demonstrated that myosin-based contraction caused both retrograde actin flow and the centripetal movement of fibronectin-coated beads (32), and Giannone et al. have shown that lamellipodia undergo periodic contractile waves associated with rearward actin flow (35). These data support our finding that peripheral regions of the cell transition from compressive strain toward tensile strain.

The apparent importance of regional, subcellular regulation of traction forces for fibronectin matrix assembly has implications for the role of environmental or substrate stiffness in this process. If increased pulling force directly resulted in larger fibril formation and there was no requirement for gradients of traction force across the cell, then stiff substrates should be ideal for matrix assembly, whereas assembly of fibrils on soft substrates would be substantially more difficult. Any given level of myosin activation would lead to greater force generation and more efficient matrix assembly in cells attached to a stiff substrate than in cells on a soft substrate. However, studies of fibrillogenesis on poly(vinyl alcohol) or glass substrates that were both coated with covalently bound fibronectin show that fibroblasts assembled long fibronectin fibrils when plated onto soft substrates, but no fibrils were assembled on stiffer glass substrates (36). These findings support our hypothesis that
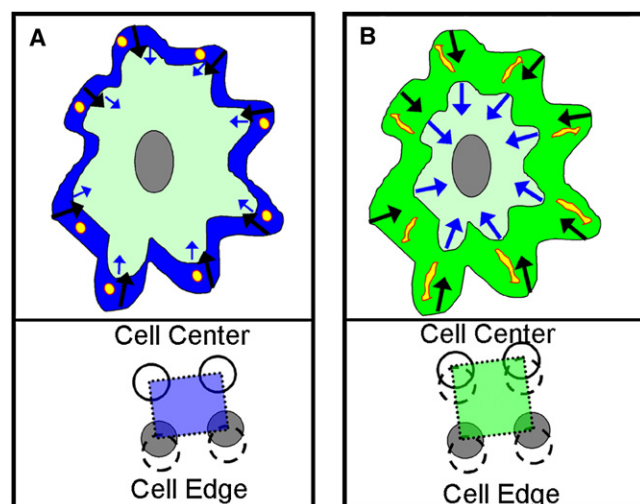
FIGURE 6 Schematic of force and strain transitions in fibronectin fibrillogenesis. Changes in the distribution of traction forces lead to local variations in strain, which facilitate assembly of fibronectin. (*A, upper*) Initially, traction forces are largest at the cell periphery (*black vectors*) and smaller toward the cell center (*blue vectors*), leading to compressive strain at the cell periphery (*blue perimeter*) and abetting fibronectin fibril nucleation (*red-outlined yellow circles*). A representative quadrant of four posts (*A, lower*) shows how large peripheral forces and small interior forces mediate compressive strain in the quadrant. (*B, upper*) Subsequently, traction forces closer to the cell center (*blue vectors*) increase as peripheral forces (*black vectors*) decrease. This new traction force pattern creates a transition from compressive to neutral strain (*green*) in the cell periphery, stretching the nascent fibronectin fibrils. A representative quadrant of four posts (*B, lower*) demonstrates how equal peripheral and interior forces result in neutral strain. Note that forces are still present in the neutral strain scenario, but are equal in size. Posts are represented as circles (*gray*, peripheral post tops; *white*, interior post tops; *dashed circles*, post bases). The directions of the cell center and cell edge are labeled in the lower panels to indicate the orientation of the posts within a cell.

spatially graded differences in traction force that are available on softer substrates facilitate fibronectin assembly.

The mechanistic insights provided by this study into the way in which modulation of myosin-based contractility affects matrix patterning has important implications for vascular biology and medicine. Chronic upregulation of Rho kinase activity is a common theme in molecular dysregulation that underlies defective vascular remodeling and wound healing responses in diabetes and hypertension (37). Our data indicate that effective therapeutic strategies for these issues must go beyond simple tonic inhibition of the kinases that regulate cytoskeletal contraction. It may instead be necessary to restore the physiologic cycling and subcellular segmentation of cytoskeletal responses shown here to be integral to the optimal patterning of the fibronectin matrix. These studies therefore lend what we believe are new insights into the process of matrix assembly and the ways in which dynamic transitions in cell traction force topography and compressive strain at the cell-matrix interface change during the formation of matrix fibrils.

SUPPORTING MATERIAL

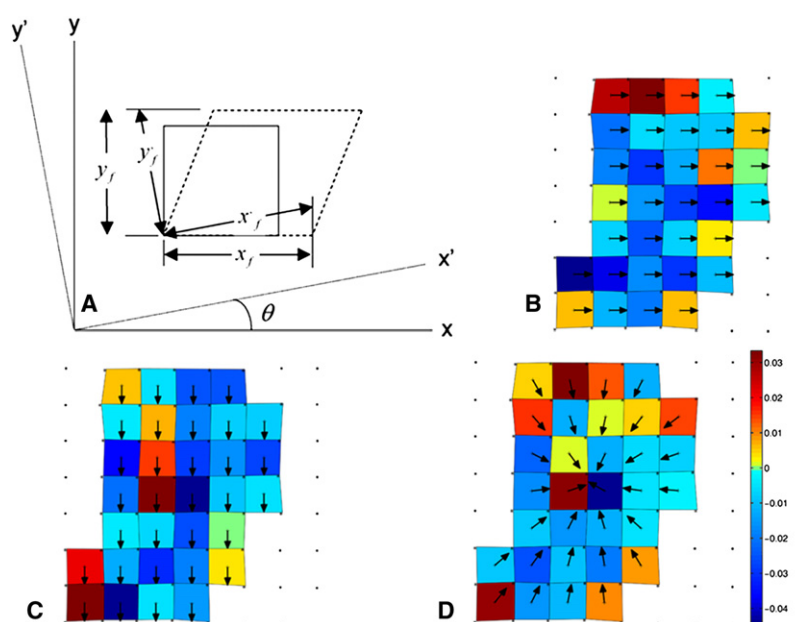Two figures are available at www.biophys.org/BPJ/supplemental/S0006-3495(08)00059-3.

FIGURE 7 Strain calculations and transformations. (*A*) Transformation of strains can be used to calculate element strain in any arbitrary coordinate system. (*B–D*) A representative strain map showing (*B*) strain in the *x* direction, (*C*) strain in the *y* direction, and (*D*) centripetally directed strain. Tensile strains yield positive values, whereas compressive strains yield negative values. Black arrows represent the direction in which strain was calculated.

REFERENCES

1. George, E. L., E. N. Georges-Labouesse, R. S. Patel-King, H. Rayburn, and R. O. Hynes. 1993. Defects in mesoderm, neural tube and vascular development in mouse embryos lacking fibronectin. *Development.* 119:1079–1091.

2. Mosher, D. F., F. J. Fogerty, M. A. Chernousov, and E. L. Barry. 1991. Assembly of fibronectin into extracellular matrix. *Ann. N. Y. Acad. Sci.* 614:167–180.

3. Ohashi, T., D. P. Kiehart, and H. P. Erickson. 2002. Dual labeling of the fibronectin matrix and actin cytoskeleton with green fluorescent protein variants. *J. Cell Sci.* 115:1221–1229.

4. Chen, L. B., A. Murray, R. A. Segal, A. Bushnell, and M. L. Walsh. 1978. Studies on intercellular LETS glycoprotein matrices. *Cell.* 14:377–391.

5. Singer, I. I. 1979. The fibronexus: a transmembrane association of fibronectin-containing fibers and bundles of 5 nm microfilaments in hamster and human fibroblasts. *Cell.* 16:675–685.

6. Hocking, D. C., J. Sottile, and P. J. McKeown-Longo. 1994. Fibronectin's III-1 module contains a conformation-dependent binding site for the amino-terminal region of fibronectin. *J. Biol. Chem.* 269:19183–19187.

7. Chernousov, M. A., A. I. Faerman, M. G. Frid, O. Printseva, and V. E. Koteliansky. 1987. Monoclonal antibody to fibronectin which inhibits extracellular matrix assembly. *FEBS Lett.* 217:124–128.

8. Zhong, C., M. Chrzanowska-Wodnicka, J. Brown, A. Shaub, A. M. Belkin, et al. 1998. Rho-mediated contractility exposes a cryptic site in fibronectin and induces fibronectin matrix assembly. *J. Cell Biol.* 141:539–551.

9. Gao, M., D. Craig, O. Lequin, I. D. Campbell, V. Vogel, et al. 2003. Structure and functional significance of mechanically unfolded fibronectin type III1 intermediates. *Proc. Natl. Acad. Sci. USA.* 100:14784–14789.

10. Ohashi, T., D. P. Kiehart, and H. P. Erickson. 1999. Dynamics and elasticity of the fibronectin matrix in living cell culture visualized by fibronectin-green fluorescent protein. *Proc. Natl. Acad. Sci. USA.* 96:2153–2158.

11. Davidson, L. A., B. D. Dzamba, R. Keller, and D. W. Desimone. 2008. Live imaging of cell protrusive activity, and extracellular matrix assembly and remodeling during morphogenesis in the frog, *Xenopus laevis. Dev. Dynam.* 237:2684–2692.

12. Smith, M. L., D. Gourdon, W. C. Little, K. E. Kubow, R. A. Eguiluz, et al. 2007. Force-induced unfolding of fibronectin in the extracellular matrix of living cells. *PLoS Biol.* 5, e268.

13. Baneyx, G., L. Baugh, and V. Vogel. 2002. Fibronectin extension and unfolding within cell matrix fibrils controlled by cytoskeletal tension. *Proc. Natl. Acad. Sci. USA.* 99:5139–5143.

14. Erickson, H. P. 2002. Stretching fibronectin. *J. Muscle Res. Cell Motil.* 23:575–580.

15. Abu-Lail, N. I., T. Ohashi, R. L. Clark, H. P. Erickson, and S. Zauscher. 2006. Understanding the elasticity of fibronectin fibrils: unfolding strengths of FN-III and GFP domains measured by single molecule force spectroscopy. *Matrix Biol.* 25:175–184.

16. Burridge, K., and M. Chrzanowska-Wodnicka. 1996. Focal adhesions, contractility, and signaling. *Annu. Rev. Cell Dev. Biol.* 12:463–518.

17. Harris, A. K., P. Wild, and D. Stopak. 1980. Silicone rubber substrata: a new wrinkle in the study of cell locomotion. *Science.* 208:177–179.

18. Harris, A. K., Jr. 1984. Tissue culture cells on deformable substrata: biomechanical implications. *J. Biomech. Eng.* 106:19–24.

19. Dembo, M., and Y. L. Wang. 1999. Stresses at the cell-to-substrate interface during locomotion of fibroblasts. *Biophys. J.* 76:2307–2316.

20. Tan, J. L., J. Tien, D. M. Pirone, D. S. Gray, K. Bhadriraju, et al. 2003. Cells lying on a bed of microneedles: an approach to isolate mechanical force. *Proc. Natl. Acad. Sci. USA.* 100:1484–1489.

21. Lemmon, C. A., N. J. Sniadecki, S. A. Ruiz, J. L. Tan, L. H. Romer, et al. 2005. Shear force at the cell-matrix interface: enhanced analysis for microfabricated post array detectors. *Mech. Chem. Biosyst.* 2: 1–16.

22. Otsu, N. 1979. A threshold selection method from gray-level histograms. *IEEE Trans. Syst. Man Cybern.* 9:62–66.

23. Pankov, R., E. Cukierman, B. Z. Katz, K. Matsumoto, D. C. Lin, et al. 2000. Integrin dynamics and matrix assembly: tensin-dependent translocation of $\alpha(5)\beta(1)$ integrins promotes early fibronectin fibrillogenesis. *J. Cell Biol.* 148:1075–1090.

24. Fluck, M., M. N. Giraud, V. Tunc, and M. Chiquet. 2003. Tensile stress-dependent collagen XII and fibronectin production by fibroblasts requires separate pathways. *Biochim. Biophys. Acta.* 1593:239–248.

25. Gavara, N., R. Sunyer, P. Roca-Cusachs, R. Farre, M. Rotger, et al. 2006. Thrombin-induced contraction in alveolar epithelial cells probed by traction microscopy. *J. Appl. Physiol.* 101:512–520.

26. Limouze, J., A. F. Straight, T. Mitchison, and J. R. Sellers. 2004. Specificity of blebbistatin, an inhibitor of myosin II. *J. Muscle Res. Cell Motil.* 25:337–341.

27. Chartier, L., L. L. Rankin, R. E. Allen, Y. Kato, N. Fusetani, et al. 1991. Calyculin-A increases the level of protein phosphorylation and changes the shape of 3T3 fibroblasts. *Cell Motil. Cytoskeleton.* 18:26–40.

28. Paszek, M. J., N. Zahir, K. R. Johnson, J. N. Lakins, G. I. Rozenberg, et al. 2005. Tensional homeostasis and the malignant phenotype. *Cancer Cell.* 8:241–254.

29. Engler, A. J., S. Sen, H. L. Sweeney, and D. E. Discher. 2006. Matrix elasticity directs stem cell lineage specification. *Cell.* 126:677–689.

30. Reinhart-King, C. A., M. Dembo, and D. A. Hammer. 2005. The dynamics and mechanics of endothelial cell spreading. *Biophys. J.* 89:676–689.

31. Meshel, A. S., Q. Wei, R. S. Adelstein, and M. P. Sheetz. 2005. Basic mechanism of three-dimensional collagen fibre transport by fibroblasts. *Nat. Cell Biol.* 7:157–164.

32. Cai, Y., N. Biais, G. Giannone, M. Tanase, G. Jiang, et al. 2006. Nonmuscle myosin IIA-dependent force inhibits cell spreading and drives F-actin flow. *Biophys. J.* 91:3907–3920.

33. Brangwynne, C. P., F. C. MacKintosh, S. Kumar, N. A. Geisse, J. Talbot, et al. 2006. Microtubules can bear enhanced compressive loads in living cells because of lateral reinforcement. *J. Cell Biol.* 173: 733–741.

34. Riveline, D., E. Zamir, N. Q. Balaban, U. S. Schwarz, T. Ishizaki, et al. 2001. Focal contacts as mechanosensors: externally applied local mechanical force induces growth of focal contacts by an mDia1-dependent and ROCK-independent mechanism. *J. Cell Biol.* 153:1175–1186.

35. Giannone, G., B. J. Dubin-Thaler, H. G. Dobereiner, N. Kieffer, A. R. Bresnick, et al. 2004. Periodic lamellipodial contractions correlate with rearward actin waves. *Cell.* 116:431–443.

36. Zajaczkowski, M. B., E. Cukierman, C. G. Galbraith, and K. M. Yamada. 2003. Cell-matrix adhesions on poly(vinyl alcohol) hydrogels. *Tissue Eng.* 9:525–533.

37. Budzyn, K., P. D. Marley, and C. G. Sobey. 2006. Targeting Rho and Rho-kinase in the treatment of cardiovascular disease. *Trends Pharmacol. Sci.* 27:97–104.